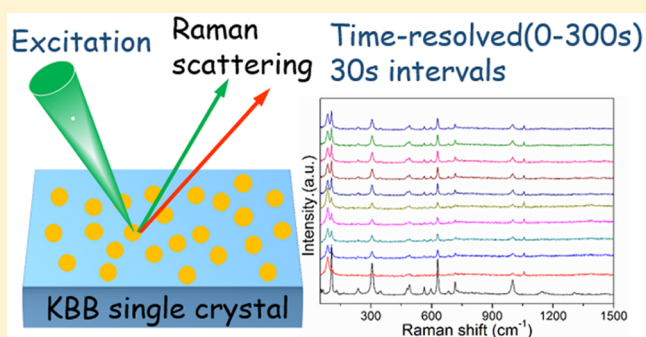


In Situ Raman Probing of Chlorphenol Degradation on Different Facets of $\text{K}_3\text{B}_6\text{O}_{10}\text{Br}$ Single Crystal

Xiaoyun Fan,^{*,†,‡} Xiu Yue,[‡] and Hanzhong Jia[‡][†]School of Environment and Guangdong Key Laboratory of Environmental Pollution and Health, Jinan University, Guangzhou 510632, China[‡]Laboratory of Environmental Sciences and Technology, Xinjiang Technical Institute of Physics & Chemistry, and Key Laboratory of Functional Materials and Devices for Special Environments, Chinese Academy of Sciences, Urumqi 830011, China

Supporting Information

ABSTRACT: Semiconductor photocatalysts with specific facets can induce high reactive activities has aroused wide attention. Here, we endeavor to gain quantitative insights into the intrinsic facet-dependent catalytic activities of $\text{K}_3\text{B}_6\text{O}_{10}\text{Br}$ (KBB) crystal using in situ Raman technique under room temperature by photocatalysis dechlorination of 2,4-DCP as a model reaction. Using a well-defined sizable KBB single crystal (size: 28 mm \times 20 mm \times 9 mm) with high (211), (110), and (101) facet exposure, the time-resolved Raman spectra for different facets have been clearly tested, it shows that the Raman spectrum of (211) facet had a remarkable change compared with (110) and (101) facets when the crystal was immersed in the 2,4-DCP solution under light irradiation. Through DFT, we obtain qualitative details on the reaction mechanisms of photocatalyzed and provide a refined understanding of the elementary processes. It was found that the $-\text{OH}$ contact mode between the pollutant and the crystal facet was the most effective mode, which can produce more $\cdot\text{OH}$ radicals than the other two modes. Moreover, the (211) facet offers the largest ratio of K atoms and surface energy, making the (211) facet more active than (110) and (101) facets.



1. INTRODUCTION

High charge-separation efficiency play an important role in the solar energy conversion process for semiconductor-based systems.¹ Photo-induced electron–hole pairs separate and transfer to the surface of a semiconductor to take part in the reaction.² Therefore, it is necessary to fully understand the charge separations during the photocatalysis process and it may also helpful to construct an efficient solar energy conversion system. Fabricating of semiconductor-based photocatalysts with preferentially exposed facets and controlled morphology has proved an efficient way of promoting photocatalytic activity in recent years.^{3,4} By tailing the surface structure at the fundamental and atomic level, various of catalysts with typical morphology has been synthesized on the nano- and microscale, and their photocatalytic properties obviously were indeed enhanced, such as, TiO_2 nanocrystals, Ag_3PO_4 submicrocrystals, BiOCl single-crystalline nanosheets, and BiVO_4 .^{5–14} However, these works were focused on the featured small size ranging from the nano- to the micrometer scale, and which facets play the exact role in photocatalysis is not well-understood yet.¹⁵ Thus, the synthesis of photocatalysts with only highly reactive facets exposed and the excellent surface atomic structures is still a great challenge.¹⁶

Polar materials^{17–20} with built-in electric fields can generate spontaneous polarization that works as a driving force for the

separation of photoinduced charges and mitigates the effect of charge recombination has arose wide attention in recent years.^{21–23} $\text{K}_3\text{B}_6\text{O}_{10}\text{Br}$ (KBB), known as a kind of borate nonlinear optical (NLO) material, demonstrated excellent catalytic activity in UV-induced dechlorination of chlorophenols, which shows a dechlorination efficiency about 2 orders of magnitude higher than that of commercial P25 TiO_2 catalyst. It was a representative work for the application of a NLO materials in the photocatalyst field.²⁴ However, most work are focus on its powdery state, very little is known regarding the shape and facet effects of KBB crystals on their photocatalytic properties. More accurately research the relationship between photocatalytic performance and facet orientation of ferroelectric material has never been reported before for the reason that it is rather difficult to grow a large size single crystal with clear exposed facet. Meanwhile, single-crystal is a great model system because of its well-defined surface, and it can be efficiently used to study the mechanism of electrochemistry, catalytic reactions, and other important surface physicochemical processes.²⁵

Received: April 4, 2018

Revised: June 4, 2018

Published: June 5, 2018



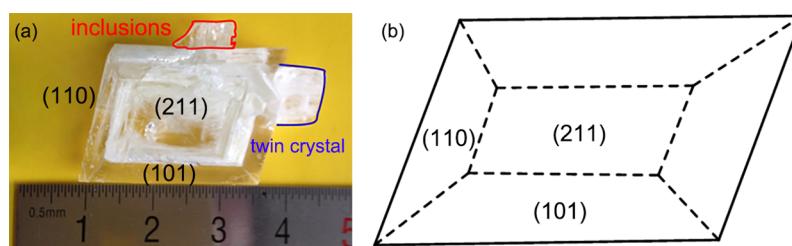


Figure 1. Images for the KBB single crystal with three predominated exposed facets (a) and the morphology of the KBB single crystal (b).

Of the many routes to study photocatalytic processes, Raman spectra can obtain useful information featured on photon-crystalline interaction by evaluating the changes of spectral peak position and the spectral width of its Raman spectra.^{26,27} Raman modes provide fingerprints in a wide range of systems and enables to track the thermodynamics and kinetics in situ photocatalytic processes, such as for adsorption and the degradation.²⁸ Therefore, Raman spectroscopy has a high molecular specificity, making it an excellent technique for materials analysis.

To this end, by adopting traditional top seed grow method, we obtain a sizable crystal with different facet to gain quantitative insights into the intrinsic facet-dependent catalytic activities of KBB crystal using the room temperature catalytic dechlorination of 2,4-DCP as a model reaction. We provided evidence by a specific intermolecular on the surface of semiconductors detected by in situ micro Raman spectroscopy under light-illumination.²⁹ We were particularly focus on the catalytic properties of high-index facet of KBB because high index facet are open surface structures with high densities of coordinately unsaturated atoms at the surface steps and kinks and thereby exhibit dramatically enhanced catalytic activities toward a variety of chemical and electrochemical reactions in comparison to the close-packed low-index facets.^{30,31} Compared with (110) and (101) facets, the Raman spectrum of the (211) facet had a remarkable change, which highly coincided with the DFT method and the photoactivities experiment results. To the best of our knowledge, this is the first time that a sizable and ferroelectric single crystal was used to test the dechlorination process of exposed facets by Raman spectroscopy.

2. EXPERIMENT

All the data were acquired as a function of time using a HORIBA Jobin Yvon LabRAM HR confocal spectrometer. The system is equipped with an automated xyz stage to allow mapping. The different crystal face was illuminated with a visible (532 nm) laser. Spectra were collected using a 50× objective (Olympus BX51) and a 100 μm confocal pinhole. All experiments used a 600 lines/mm rotatable diffraction grating along a path length of 800 mm to simultaneously scan a range of frequencies, and the spectra were detected using a SYNAPSE CCD detector (1024 pixels). The system was calibrated before collecting spectra by using a standard silicon band at 520.7 cm^{-1} . For the single crystal, spectra were acquired in the wavenumber range from 50 to 2000 cm^{-1} , with the lower limit corresponding to the cutoff of the Rayleigh rejection filter. During the tests, the z-axis position of the sample (i.e., level of sample perpendicular to optical axis) was adjusted to maximize the Raman signal.

2.1. Computational Details. The structural optimization and formation energies have been calculated using DMol3

code.^{32,33} The generalized gradient approximation (GGA) with the Perdew–Burke–Ernzerhof (PBE) functional³⁴ and all-electron double numerical basis set with polarized function (DNP) have been employed. The real-space global orbital cutoff radius is chosen to be as high as 5.1 Å. The convergence tolerance of energy is 1.0×10^{-5} Ha (1Ha = 27.21 eV), and that of maximum force is 2.0×10^{-3} Ha/Å. Each atom in the storage models is allowed to relax to the minimum in the enthalpy without any constraints. The vacuum space along the z direction is set to be 15 Å, which is enough to avoid interaction between the two neighboring images. Corrugation effects are tested and the results show that all the atoms are coplanar with each other. The calculated bulk lattice parameters of KBB are $a = b = 10.108$ Å, $c = 8.830$ Å, with k-point meshes of $5 \times 5 \times 5$.

2.2. Photocatalytic Dechlorination of 2,4-Dichlorophenol (2,4-DCP). During the experiment, the tested single crystal facet was dispersed in 30 mL of 2,4-DCP solution (50 mg/L) in a baker and stored for 10 min with stirring in the dark to attain adsorption equilibrium before under the illumination of ultraviolet light (Mercury lamp). Meantime, the other facets were coated by plasticene to avoid the contact of the 2,4-DCP solution. The percentage of residual 2,4-DCP solution at a selected time of irradiation is given by C/C_0 , where C_0 is the concentration of the 2,4-DCP solution at the initial stage, and C is the concentration at selected irradiation times (0–300 s); the interval time is 30 s. After finished the test of one surface, the next facet were washed with ethanol and water for several times, and then dried under the vacuum dryer. After that, the clean facet was adopted the same procedure as the first facet. The concentration of each chlorophenol was measured using HPLC (see [Supporting Information](#)).

3. RESULTS AND DISCUSSION

KBB single crystal with sizes up to 28 mm \times 20 mm \times 9 mm were grown by top seed grow method as previous reported.³⁵ The experiments show that facet of (211), (101), and (110) present the prominent dominance for the KBB single crystal, and there is no other facet in the present experiments as shown in [Figure 1a](#), and the morphological schematic illustrations of the as-prepared KBB samples are shown in [Figure 1b](#).

Typically, the significant regions of the Raman spectrum that are observed within 50–2,000 cm^{-1} wavenumbers. Raman spectrum of KBB single crystal with three bared surface and normalized value were shown in [Figure 2](#). It can be clearly seen that all the surfaces show a similar pattern, where only the normalized intensity was different. Raman spectrum displays strong peaks at 84, 105–107, 236, 305, 310, 491, 562, 598, 629, 686, 716, 1001, 1057, 1142, and 1311 cm^{-1} for all the crystal facets.³⁶ Normally, in a borate sample, the strong peaks at 1142–1311 cm^{-1} are attributed to the asymmetric

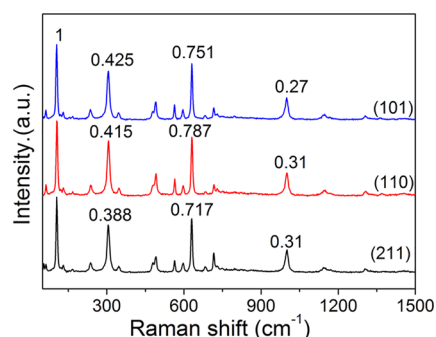


Figure 2. Normalized Raman spectrum for the three bared facets of KBB single crystal before being immersed into a 2,4-DCP solution.

stretching of B–O3, those at 1001–1057 cm^{-1} are assigned to asymmetric stretching of B–O4, the peaks around 686–716 and 629 cm^{-1} can be associated with symmetric stretching of B–O3 and B–O4, and peaks at 598 and 562 cm^{-1} were symmetric pulse vibration of triborate anion. The peaks around 491 cm^{-1} are characteristic of the bending vibration of B–O3, and the peaks around 310 and 305 cm^{-1} are assigned to the bending vibration of B–O4. The peaks below 300 cm^{-1} are attributed to the lattice vibration.³⁷ In summary, the probable vibrational bands of polyborate anions are listed in Table 1.

Table 1. Probable Vibrational Bands of Polyborate Anions

	B–O3 unit wave number (cm^{-1})	B–O4 unit wave number (cm^{-1})
asymmetric stretching	1142, 1311	1001, 1057
symmetric stretching	686, 716	629
symmetric pulse vibration	598	562
bending vibration		400–490
lattice vibration	below 310	

In order to detect the reaction effect between the pollutants and the single crystal, we adopted Raman spectroscopy to study the chemical bonds involved in degradation of these pollutants by detecting intensity and wavelength changes in the vibrational bands of these bonds, shown in Figure 3. When the UV light incident into water, they will take attenuation, in order to decrease this attenuation, we selected a small shallow container so that the single crystal just can be immersed. During the in situ experiment, the UV light was irradiated for

30 s each time then would be block off, while the Raman test was taking.

In-situ Raman results have been depicted in Figure 4. Parts a–c of Figure 4 were the images for the selected detected area under Raman spectral microscopy, where the green spot was the show of the laser irradiation site on the crystal surface. Because of the surface of single crystal was influenced when hanging out the crystal from a high temperature solution, it can be clearly see that the morphologies for the three surfaces were not smooth and obviously different. The (110) facet shows a relative smooth surface, the (101) facet exhibited a step-by-step morphology, and the (211) facet displays a rough surface. As shown in parts d–f of Figure 4, the Raman spectra of a (211) facet is obviously different from the pattern of the (110) and (010) structures. In our time-resolved degradation experiment, for the (211) facet, in the first 30 s the Raman pattern is shown to be quite different compared with the original one. For the lower frequency bond around 104 cm^{-1} , vibrations associated with lattice vibration disappeared. Meantime, some other peaks also become weak, such as the peaks around 305, 491, 627, 1001 cm^{-1} . The 1146 and 1306 cm^{-1} peaks were significantly broadened but remained at almost the same position. However, after 60 s, the spectrum maintained the same pattern. With prolonged irradiation ($t = 120$ s), the intensities of the Raman bands at 353, 564, 1146, and 1304 cm^{-1} decreased further, as time increased, after 150 s, the intensity of the Raman bands at 305, 629, and 715 cm^{-1} increased predominantly, other intensities of the Raman bands were maintained, and the broadened area disappeared. In the final stage of the degradation process ($t = 180$ –300 s), the intensities of the peaks were maintained. However, it is worth noting that obvious changes have been observed in the intensity of 308, 634, 1005 cm^{-1} peak compared with other bands, which deduced that the three weak absorption bands were not resulted from hydroxide or organic contamination of the degradation process. It has been reported that KBB has a weak Raman peak between 500 cm^{-1} .³⁸ So we were focused on the wavenumber below 500 cm^{-1} to reveal the reaction between the surface and the organic containments molecules. In the first 30 s, the intensity of the peak around 107 cm^{-1} decreased drastically; after that, the intensity increased linearly. The existence and continuous growth of the 305 cm^{-1} peak after 30 s should be related to the interaction of surface O atoms by Cl. As shown in Figure 4d, the 305 cm^{-1} Raman peak was greatly suppressed for KBB reacting in 2,4-DCP solution, especially before 30 s of reaction. This increase in lattice stress

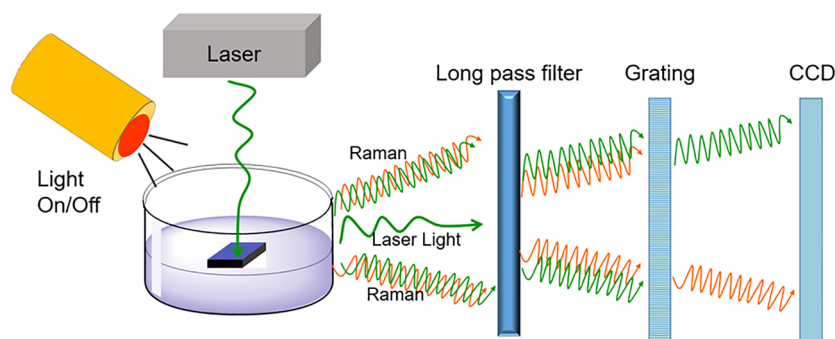


Figure 3. Schematic illustration of the experimental setup for Raman study of the KBB single crystal. KBB single crystal (cubic) was immersing into solution with blue facet as the irradiated surface, while other facets were coated by plasticene (dark surface), a mercury lamp was used as the light source.

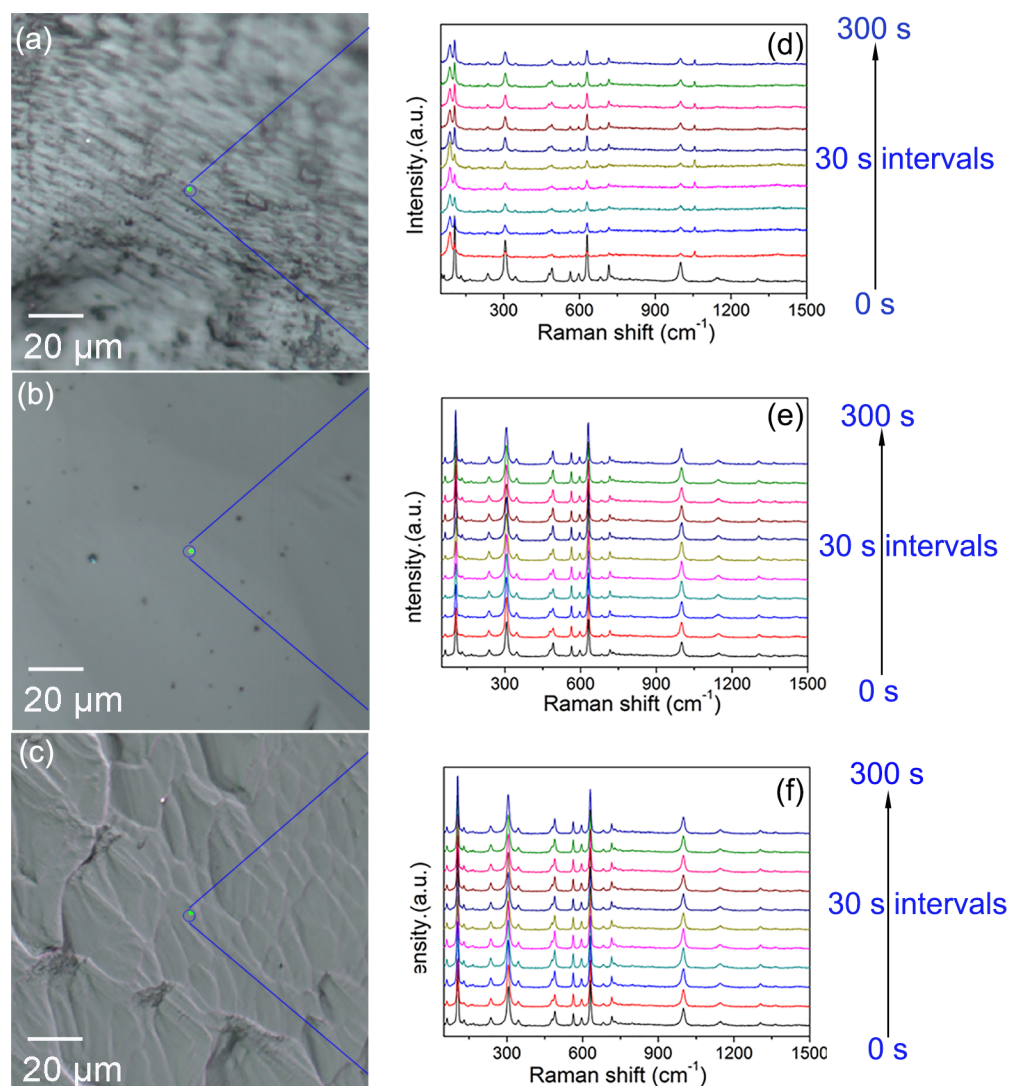


Figure 4. Images of the three facets from Raman microscope (a–c), and the corresponding Raman spectrum (d–f) for (211), (110), and (101) facets, respectively.

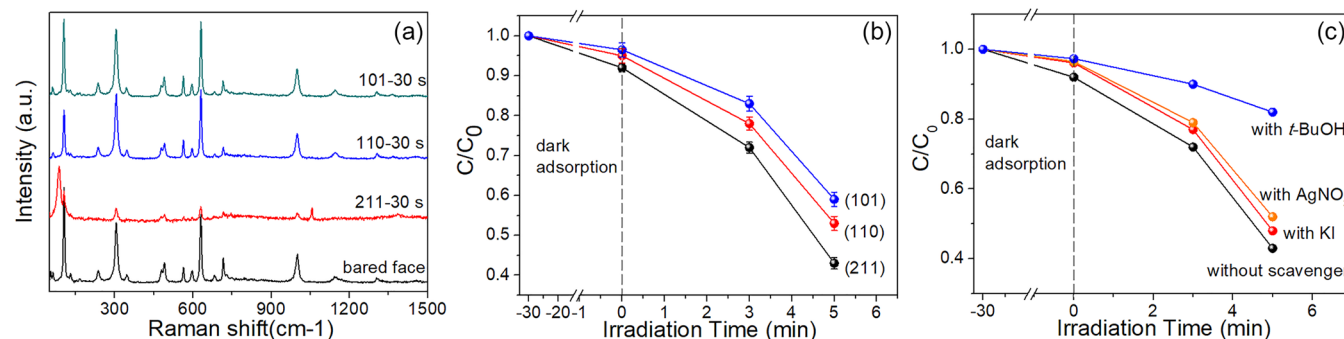


Figure 5. Raman spectrum changes for the first 30 s (a) and Photocatalytic dechlorination of 2,4-DCP (50 mg L⁻¹, 30 mL) (b) on three different exposed facets, while the other two facets were coated with plasticene. Degradation curves of 2,4-DCP with different scavengers on (211) facet under the UV light irradiation (c).

can also be attributed to the replacement of oxygen atoms by the chlorine atom.³⁹ The reason for the increase of the 84, 104, and 240 cm⁻¹ peaks at different time points can be associated with the induced expression of contact atoms. Precise assignment of three bands have not been achieved at present, and we conjecture that they are probably due to overtone or

combination bands from the boron–oxygen modes. These three bands were assigned to the channel breathing vibrational modes and deformations involving the four-membered rings, respectively. And the dechlorination step was followed by dehydrogenation to generate benzoquinone, which could also be confirmed by the color changes of suspensions from

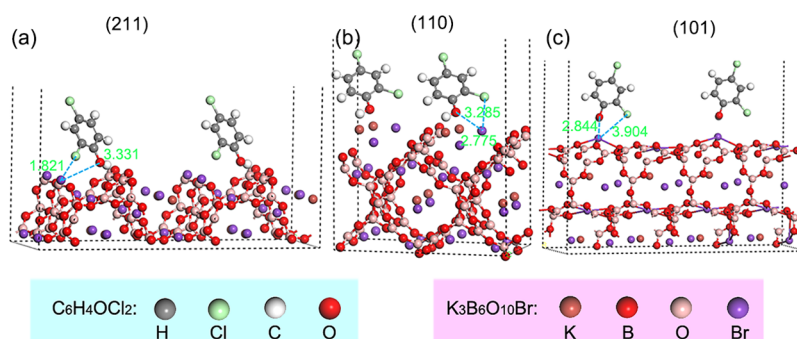


Figure 6. Adsorption configurations for the three different facets between 2,4-DCP and KBB single crystal facets (211) (a), (110) (b), and (101) (c).

transparent to light yellow (Figure S1 in the Supporting Information). Subsequently, the ring of benzoquinone was opened by the further oxidation of $\bullet\text{OH}$ to form aliphatic carboxylic acids and so on.⁴⁰ However, the patterns for (110) and (101) facets did not show significant changes for the weak interactions between surface atoms and the 2,4-DCP molecular, shown in Figure 4e,f. Therefore, it is need to consider the relationship between photo activity and the surface structure of three facets.

From Raman result, we can clearly see that the (211) facet shows an obvious shift compared with the other two facets when immersing into 2,4-DCP solutions, see in Figure 5a. In order to determine the relationship for facet-dependent photocatalytic activity of KBB, the photocatalytic degradation of chlorophenol on (211), (110), and (101) facets were investigated. Same size area for each exposed facet was selected to avoid surface area difference. The area size is $1.0\text{ cm} \times 1.0\text{ cm} = 1\text{ cm}^2$ for (211) and (101) facets, while due to the narrow width of the (110) facet, we selected different patterns as $2.0\text{ cm} \times 0.5\text{ cm} = 1\text{ cm}^2$ to maintain the same area size. The (211) facet exhibits a dramatically higher degradation rate, about 3 and 5 times higher than the (110) and (101) facets in the first 6 min, respectively, as shown in Figure 5b. We did not prolong the time as in the previous work, due to the small container with almost 30 mL of 2,4-DCP solution. Furthermore, the photogenerated reactive species was explored using AgNO_3 , $t\text{-BuOH}$, and KI as scavenger of electrons (e^-), $\bullet\text{OH}$, and hole (h^+), respectively. Addition of excess AgNO_3 and KI show a neglect effect on the degradation of 2,4-DCP. However, the decomposition of 2,4-DCP was significantly inhibited by addition of $t\text{-BuOH}$ compared with no scavenger under the same conditions, indicating that the 2,4-DCP photodegradation is proceeded by $\bullet\text{OH}^-$ to a large degree, shown in Figure 5c.

To further clarify the underlying mechanism for the higher photocatalytic activity of (211) facet relative to (110) and (101) facets, we further studied the surface structures and surface energies of the (211), (110), and (101) facets through density functional theory (DFT) calculations.⁴¹ During the photocatalytic processes, a DFT method can provide a detailed thermodynamic analysis as well as structural and kinetic information.⁴¹ The relaxed unit cells used to construct the surface models are shown in Figure 6. The activity of the surface is strongly related to the value of the surface free energy. Surfaces with a low surface energy are usually stable and easy to form experimentally, but they are unlikely to be reactive. On the other hand, surfaces with high surface energy are usually unstable, active, and easy to be reconstructed in the

experiment. The exact calculation results show that the surface energy of the (211) facets is calculated to be 8.962 eV/nm^2 , which is higher than that of (110) (ca. 7.60 eV/nm^2) and (101) (ca. 3.312 eV/nm^2) facets, indicating that the (211) facet of KBB are more reactive than the (110) and (101) facets, and thus it should facilitate the 2,4-DCP adsorption and provide more catalytically active sites.

As photocatalytic reactions happen at the surface of the photocatalysts, the atomic arrangement of semiconductor surface significantly influences their surface properties,⁴² thus the difference in surface atomic structures may lead to the discrepancy in the ability of chemisorbed oxygen species or $\bullet\text{OH}$.^{43,44} We therefore find that the photocatalytic reactivity of KBB are strong influence by surface of K atoms density. DFT simulation shows that the surface with higher K-terminated ratio surfaces generally have surface energy much higher than that of higher ration of O or B terminated surfaces, which is consistent with the fact that KBB surfaces with high ratio exposed of K atoms are more reactive. From the calculation, the results suggest that the (211) facet is mainly constituted by K atoms and has a relatively higher surface energy than (110) and (101) facets, and thus they are very favorable for enhancing the photocatalytic activities of KBB facets. The atoms ratio for different facets were shown in Table 2. On the other hand, from the different view direction for the

Table 2. Atomic Ratio on Different Surfaces for the KBB Single Crystal

surface structure	K (%)	B (%)	O (%)	Br (%)
(211)	30	30	30	10
(110)	16.7	33.3	33.3	16.7
(101)	7.7	38.5	53.8	0

KBB (in the Supporting Information in Figures S2–S4), it can be clearly seen that for (211) facet the crystal has a three-dimensional structure with K and Br atoms loosely distributed in the large tunnel. It will be convenient for the charges to separate; however, for the (110) and (101) facets, all the atoms are packed thickly. When the surface is under irradiation, the charges will be easily trapped and therefore, it drives the reaction to electron transfer.

We next considered three contact modes for the 2,4-DCP molecular and the KBB crystals (Figure 7), they are, the KBB surface with contact with vertical $-\text{Cl}$ group, vertical $-\text{OH}$ group, and the flat plan mode. The values of the adsorption energy (E_{ads}) can be measured which is a magnitude of the binding strength indicate the adsorption ability of molecular

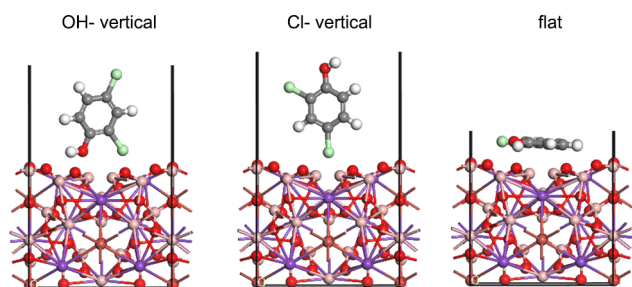


Figure 7. Three different adsorbed modes for 2,4-DCP molecular on KBB single crystal.

species on crystal surfaces, shown in Table 3. The noticeable distinction of the E_{ads} for the (211) facet when contacted with

Table 3. Absorption Energy for Different Adsorption Modes of the 2,4-DCP Molecule on the KBB Single Crystal

surface structure	adsorbed mode of 2,4- DCP molecular (eV/nm ²)		
	flat	vertical-Cl	vertical-OH
(211)	−0.436	−0.245	−0.572
(110)	−0.599	−0.517	−0.789
(101)	−0.435	−0.299	−0.517

the vertical −OH group is −0.572 eV, while the value for the vertical −Cl group and flat plan mode are −0.245 and −0.436 eV, respectively. It means that chlorophenol adsorption on the (211) facet with vertical −OH group overcame the smallest energy barrier compared with that on (101) and (110) facets, resulting in the highest chlorophenol adsorption on the (211) facet. Therefore, the vertical −OH state is the most stable contact mode compared with the −Cl and plan mode when adsorbed on the surface of KBB crystal, further indicating that 2,4-DCP prefers to be adsorbed at the (211) facet with the mode of −OH binding.

For the K–O bonds, the minimum electron density at the bond decreased with increasing bond length.⁴⁵ Because of the DFT can be employed to identify active sites in the functionalization step via readily computed parameters. One of the simplest parameters available is charge.²² Atomic charges could potentially reveal the most electrophilic sites and hence predict sites of attack by nucleophilic radicals and vice versa. We set out to determine whether atomic charge could be a reliable predictor of site selectivity, since positive charge would make carbon atoms more susceptible to nucleophilic radical attacks. The overall results show that the predicted activated sites based on atomic charges are in generally good agreement with the corresponding experimentally determined products, see Figure 8.

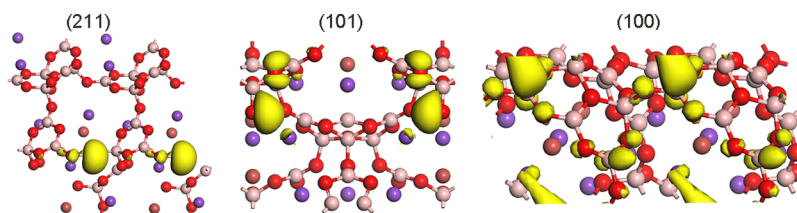


Figure 8. Plots of the electron density difference of 2,4- DCP molecules adsorbed on the (211), (100), and (101) surfaces of the KBB catalyst. Orange color indicates the electron density.

On the basis of the above calculations, we speculate that KBB (211) possesses a high density of K atoms, which may markedly increase the number of catalytically active sites on their surfaces and facilitate the adsorption of 2,4-DCP molecules on these sites, thus promoting the chlorophenol adsorption. Thereby, the degradation reaction between the adsorbed organic pollutants molecules and photogenerated holes could proceed more rapidly under ultraviolet light irradiation, which may result in a higher photocatalytic activity for the degradation of organic pollutants. Furthermore, for the bulk facets, the spatially separated O and B atomic layers could effectively facilitate the separation and transfer of photo-generated electron–hole pairs.⁹ The ability of absorbing oxygen species is obviously depend on the density of K atoms.⁴⁶ On the other hand, the (211) stacking consists of metal and oxygen ions, which generate an electrostatic dipole field perpendicular to the surface, and the surface energy of bulk-terminated polar surface diverges with respect to slab thickness.²⁹

Therefore, the possible reasons for the high activity of the (211) facet to degradation of 2,4-DCP molecules can be summarized as follows. First, the (211) facet offers largest ratio of K atoms capable of forming terminal K–OH species, which in turn promotes the adsorption of chlorophenol on the facets via $\bullet\text{OH}\cdots\pi$ -electron-type interaction.³⁷ Second, the contact mode by hydroxyl groups on the (211) facet plays an important role in chlorophenol degradation because hydroxyl groups directly participate in the degradation process by trapping the charge carriers to produce very reactive $\bullet\text{OH}$ radicals, making the (211) facet an oxidation site to generate more $\bullet\text{OH}$ radicals. During the photocatalytic process, the molecularly water is probably continuing dissociated to form hydroxyls and further promote the degradation rate. Third, the largest surface energy make (211) facet surface are more reactive and thus it should facilitate the 2,4-DCP adsorption and provide more catalytically active sites. These synergetic effects of surface adsorption are mainly responsible for the superiority of (211) facet in comparison with (110) and (101) facets in chlorophenol degradation, as shown in Figure 9. We present computational evidence and details in favor of the established reaction mechanism. KBB single crystal with different facets⁴⁷ have been successfully prepared and the photocatalytic performance of the different surface was investigated. However, facet-specific charge transfer may not be the sole cause of the improved photocatalytic activity.

4. CONCLUSIONS

In conclusion, by using in situ Raman spectroscopy, a clear reversible correlation between different single crystal facet and the pollutants was observed. Through DFT, we obtain qualitative details on the reaction mechanisms of photo-

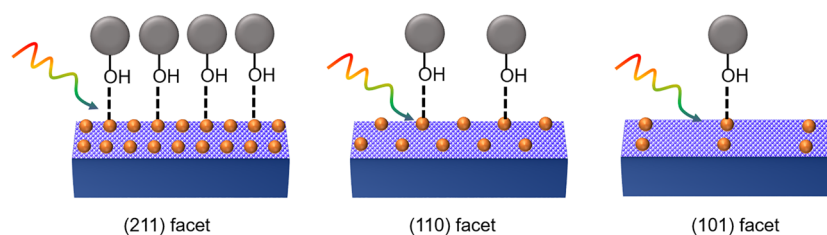


Figure 9. Superiority of the (211) facet in comparison with (110) and (101) facets in 2,4-DCP degradation. The blue cube represents the KBB single crystal, and the yellow sphere and gray sphere represent K atoms and chlorophenol units, respectively.

catalyzed transformations and provide a refined understanding of the elementary processes involved. Moreover, we have demonstrated that relatively straightforward calculations of atomic charges of site activity in photoactivity systems are possible. This in situ method offers unique opportunities for studying the reactions between organic pollutants on different crystal facet. From the presented method, we expect it to gain widespread use in mechanistic investigations and the optimization of water system reactions for photocatalysts.

■ ASSOCIATED CONTENT

● Supporting Information

The Supporting Information is available free of charge on the ACS Publications website at DOI: [10.1021/acs.jpcc.8b03176](https://doi.org/10.1021/acs.jpcc.8b03176).

Detailed experimental procedures for photocatalytic dechlorination of 2,4-dichlorophenol, color change of the 2,4-DCP solution, and view of the structure of KBB along the (211), (110), and (101) directions of the KBB catalyst (PDF)

■ AUTHOR INFORMATION

Corresponding Author

*(X.F.) E-mail: xyfan@jun.edu.cn.

ORCID

Xiaoyun Fan: 0000-0002-4213-8329

Hanzhong Jia: 0000-0003-1842-4218

Notes

The authors declare no competing financial interest.

■ ACKNOWLEDGMENTS

This work was supported by the National Natural Science Foundation of China (51772325), CAS Youth Innovation Promotion Association (2017473), “Western Light” Program of Chinese Academy of Sciences (YBXM 201401), and Natural Science Foundation of Xinjiang Uygur Autonomous Region (2016D01A072).

■ REFERENCES

- (1) Chen, X.; Shen, S.; Guo, L.; Mao, S. S. Semiconductor-Based Photocatalytic Hydrogen Generation. *Chem. Rev.* **2010**, *110*, 6503–6570.
- (2) Wang, H.; Zhang, L.; Chen, Z.; Hu, J.; Li, S.; Wang, Z.; Liu, J.; Wang, X. Semiconductor Heterojunction Photocatalysts: Design, Construction, and Photocatalytic Performances. *Chem. Soc. Rev.* **2014**, *43*, 5234–5244.
- (3) Atwater, H. A.; Polman, A. Plasmonics for Improved Photovoltaic Devices. *Nat. Mater.* **2010**, *9*, 865–865.
- (4) Bi, Y.; Ouyang, S.; Umezawa, N.; Cao, J.; Ye, J. Facet Effect of Single-Crystalline Ag_3PO_4 Sub-Microcrystals on Photocatalytic Properties. *J. Am. Chem. Soc.* **2011**, *133*, 6490–6492.
- (5) Tachikawa, T.; Ochi, T.; Kobori, Y. Crystal-Face-Dependent Charge Dynamics on a BiVO_4 Photocatalyst Revealed by Single-Particle Spectroelectrochemistry. *ACS Catal.* **2016**, *6*, 2250–2256.
- (6) Dong, F.; Xiong, T.; Yan, S.; Wang, H.; Sun, Y.; Zhang, Y.; Huang, H.; Wu, Z. Facets and Defects Cooperatively Promote Visible Light Plasmonic Photocatalysis with Bi Nanowires@ BiOCl Nanosheets. *J. Catal.* **2016**, *344*, 401–410.
- (7) Chen, Y.; Zhao, H.; Liu, B.; Yang, H. Charge Separation between Wurtzite ZnO Polar {001} Surfaces and Their Enhanced Photocatalytic Activity. *Appl. Catal., B* **2015**, *163*, 189–197.
- (8) Shi, R.; Wang, Y.; Li, D.; Xu, J.; Zhu, Y. Synthesis of ZnWO_4 Nanorods with [100] Orientation and Enhanced Photocatalytic Properties. *Appl. Catal., B* **2010**, *100*, 173–178.
- (9) Liu, X.; Dong, G.; Li, S.; Lu, G.; Bi, Y. Direct Observation of Charge Separation on Anatase TiO_2 Crystals with Selectively Etched {001} Facets. *J. Am. Chem. Soc.* **2016**, *138*, 2917–2920.
- (10) Li, C.; Koenigsmann, C.; Ding, W.; Rudsteyn, B.; Yang, K. R.; Regan, K. P.; Konezny, S. J.; Batista, V. S.; Brudvig, G. W.; Schmuttenmaer, C. A.; Kim, J.-H. *J. Am. Chem. Soc.* **2015**, *137*, 1520–1529.
- (11) Zhao, Y.; Zhang, Y.; Liu, H.; Ji, H.; Ma, W.; Chen, C.; Zhu, H.; Zhao, J. Control of Exposed Facet and Morphology of Anatase Crystals through TiOx Precursor Synthesis and Impact of the Facet on Crystal Phase Transition. *Chem. Mater.* **2014**, *26*, 1014–1018.
- (12) Huang, H.; He, Y.; Li, X.; Li, M.; Zeng, C.; Dong, F.; Du, X.; Zhang, T.; Zhang, Y. $\text{Bi}_2\text{O}_2(\text{OH})(\text{NO}_3)$ as a Desirable $[\text{Bi}_2\text{O}_2]^{2+}$ Layered Photocatalyst: Strong Intrinsic Polarity, Rational Band Structure and {001} Active Facets Co-Beneficial for Robust Photooxidation Capability. *J. Mater. Chem. A* **2015**, *3*, 24547–24556.
- (13) Li, R.; Zhang, F.; Wang, D.; Yang, J.; Li, M.; Zhu, J.; Zhou, X.; Han, H.; Li, C. Spatial Separation of Photogenerated Electrons and Holes among {010} and {110} Crystal Facets of BiVO_4 . *Nat. Commun.* **2013**, *4*, 1432.
- (14) Chen, Z.; Wang, W.; Zhang, Z.; Fang, X. High-Efficiency Visible-Light-Driven $\text{Ag}_3\text{PO}_4/\text{AgI}$ Photocatalysts: Z-Scheme Photocatalytic Mechanism for Their Enhanced Photocatalytic Activity. *J. Phys. Chem. C* **2013**, *117*, 19346–19352.
- (15) Zhu, J.; Pang, S.; Dittrich, T.; Gao, Y.; Nie, W.; Cui, J.; Chen, R.; An, H.; Fan, F.; Li, C. Visualizing the Nano Cocatalyst Aligned Electric Fields on Single Photocatalyst Particles. *Nano Lett.* **2017**, *17*, 6735–6741.
- (16) Yang, Y.-C.; Xu, L.; Huang, W.-Q.; Luo, C.-Y.; Huang, G.-F.; Peng, P. Electronic Structures and Photocatalytic Responses of $\text{SrTiO}_3(100)$ Surface Interfaced with Graphene, Reduced Graphene Oxide, and Graphane: Surface Termination Effect. *J. Phys. Chem. C* **2015**, *119*, 19095–19104.
- (17) Lou, Z.; Wang, P.; Huang, B.; Dai, Y.; Qin, X.; Zhang, X.; Wang, Z.; Liu, Y. Enhancing Charge Separation in Photocatalysts with Internal Polar Electric Fields. *ChemPhotoChem.* **2017**, *1*, 136–147.
- (18) Zhang, Q.; An, Q.; Luan, X.; Huang, H.; Li, X.; Meng, Z.; Tong, W.; Chen, X.; Chu, P. K.; Zhang, Y. Achieving Significantly Enhanced Visible-Light Photocatalytic Efficiency Using a Polyelectrolyte: The Composites of Exfoliated Titania Nanosheets, Graphene, and Poly(Diallyl-Dimethyl-Ammonium Chloride). *Nanoscale* **2015**, *7*, 14002–14009.
- (19) Li, L.; Salvador, P. A.; Rohrer, G. S. Photocatalysts with Internal Electric Fields. *Nanoscale* **2014**, *6*, 24–42.

- (20) Huang, H.; Tu, S.; Zeng, C.; Zhang, T.; Reshak, A. H.; Zhang, Y. Macroscopic Polarization Enhancement Promoting Photo- and Piezoelectric-Induced Charge Separation and Molecular Oxygen Activation. *Angew. Chem., Int. Ed.* **2017**, *56*, 11860–11864.
- (21) Fan, X.; Wu, Z.; Wang, L.; Wang, C. Exploring the Origin of High Dechlorination Activity in Polar Materials $M_2B_3O_9Cl$ ($M = Ca, Sr, Ba, Pb$) with Built-in Electric Field. *Chem. Mater.* **2017**, *29*, 639–647.
- (22) Fan, X.; Lai, K.; Wang, L.; Qiu, H.; Yin, J.; Zhao, P.; Pan, S.; Xu, J.; Wang, C. Efficient Photocatalytic Dechlorination of Chlorophenols over a Nonlinear Optical Material $Na_3VO_2B_6O_{11}$ under Uv-Visible Light Irradiation. *J. Mater. Chem. A* **2015**, *3*, 12179–12187.
- (23) Fan, X.; Liu, J.; Lai, K.; Wang, C. $K_3Mb_5O_{10}$ ($M = Zn$ and Cd) with d10 Configuration: Efficient and Reusable Catalysts for Dehalogenation of Halophenols. *Appl. Catal., B* **2017**, *206*, 599–607.
- (24) Fan, X.; Zang, L.; Zhang, M.; Qiu, H.; Wang, Z.; Yin, J.; Jia, H.; Pan, S.; Wang, C. A Bulk Boron-Based Photocatalyst for Efficient Dechlorination: $K_3B_6O_{10}Br$. *Chem. Mater.* **2014**, *26*, 3169–3174.
- (25) Liu, S.; Yu, J.; Jaroniec, M. Tunable Photocatalytic Selectivity of Hollow TiO_2 Microspheres Composed of Anatase Polyhedra with Exposed {001} Facets. *J. Am. Chem. Soc.* **2010**, *132*, 11914–11916.
- (26) Li, J.-F.; Zhang, Y.-J.; Ding, S.-Y.; Panneerselvam, R.; Tian, Z.-Q. Core–Shell Nanoparticle-Enhanced Raman Spectroscopy. *Chem. Rev.* **2017**, *117*, 5002–5069.
- (27) Kawata, S.; Ichimura, T.; Taguchi, A.; Kumamoto, Y. Nano-Raman Scattering Microscopy: Resolution and Enhancement. *Chem. Rev.* **2017**, *117*, 4983–5001.
- (28) Zhang, H.; Guo, L.-H.; Zhao, L.; Wan, B.; Yang, Y. Switching Oxygen Reduction Pathway by Exfoliating Graphitic Carbon Nitride for Enhanced Photocatalytic Phenol Degradation. *J. Phys. Chem. Lett.* **2015**, *6*, 958–963.
- (29) Chen, B.; Yang, M.; Priya, S.; Zhu, K. Origin of J–V Hysteresis in Perovskite Solar Cells. *J. Phys. Chem. Lett.* **2016**, *7*, 905–917.
- (30) Jiao, Z.; Zhang, Y.; Yu, H.; Lu, G.; Ye, J.; Bi, Y. Concave Trisoctahedral Ag_3PO_4 Microcrystals with High-Index Facets and Enhanced Photocatalytic Properties. *Chem. Commun.* **2013**, *49*, 636–638.
- (31) Kuang, Q.; Wang, X.; Jiang, Z.; Xie, Z.; Zheng, L. High-Energy-Surface Engineered Metal Oxide Micro- and Nanocrystallites and Their Applications. *Acc. Chem. Res.* **2014**, *47*, 308–318.
- (32) Delley, B. An All-Electron Numerical Method for Solving the Local Density Functional for Polyatomic Molecules. *J. Chem. Phys.* **1990**, *92*, 508–517.
- (33) Delley, B. From Molecules to Solids with the DMol₃ Approach. *J. Chem. Phys.* **2000**, *113*, 7756–7764.
- (34) Perdew, J. P.; Burke, K.; Ernzerhof, M. Generalized Gradient Approximation Made Simple. *Phys. Rev. Lett.* **1996**, *77*, 3865–3868.
- (35) Fan, X.; Zhang, M.; Pan, S.; Yang, Y.; Zhao, W. Top Seeded Solution Growth and Optical Properties of a Bromic Borate Crystal: $K_3B_6O_{10}Br$. *Mater. Lett.* **2012**, *68*, 374–377.
- (36) Jun, L.; Shuping, X.; Shiyang, G. FT-IR and Raman Spectroscopic Study of Hydrated Borates. *Spectrochim. Acta, Part A* **1995**, *51*, 519–532.
- (37) Zhihong, L.; Bo, G.; Mancheng, H.; Shuni, L.; Shuping, X. FT-IR and Raman Spectroscopic Analysis of Hydrated Cesium Borates and Their Saturated Aqueous Solution. *Spectrochim. Acta, Part A* **2003**, *59*, 2741–2745.
- (38) Kamitsos, E. I.; Karakassides, M. A.; Chrysikos, G. D. Vibrational spectra of magnesium-sodium-borate glasses. 2. Raman and mid-infrared investigation of the network structure. *J. Phys. Chem.* **1987**, *91*, 1073–1079.
- (39) Ma, L.; Liu, M.; Jing, D.; Guo, L. Photocatalytic Hydrogen Production over CdS: Effects of Reaction Atmosphere Studied by in Situ Raman Spectroscopy. *J. Mater. Chem. A* **2015**, *3*, 5701–5707.
- (40) Lan, S.; Feng, J.; Xiong, Y.; Tian, S.; Liu, S.; Kong, L. Performance and Mechanism of Piezo-Catalytic Degradation of 4-Chlorophenol: Finding of Effective Piezo-Dechlorination. *Environ. Sci. Technol.* **2017**, *51*, 6560–6569.
- (41) Demissie, T. B.; Hansen, J. H. Mechanism and Site Selectivity in Visible-Light Photocatalyzed C-H Functionalization: Insights from DFT Calculations. *J. Org. Chem.* **2016**, *81*, 7110–7120.
- (42) Wen, F.; Li, C. Hybrid Artificial Photosynthetic Systems Comprising Semiconductors as Light Harvesters and Biomimetic Complexes as Molecular Cocatalysts. *Acc. Chem. Res.* **2013**, *46*, 2355–2364.
- (43) Chin, Y.-H.; Buda, C.; Neurock, M.; Iglesia, E. Reactivity of Chemisorbed Oxygen Atoms and Their Catalytic Consequences During CH_4 - O_2 Catalysis on Supported Pt Clusters. *J. Am. Chem. Soc.* **2011**, *133*, 15958–15978.
- (44) Wang, M.; Zhang, F.; Zhu, X.; Qi, Z.; Hong, B.; Ding, J.; Bao, J.; Sun, S.; Gao, C. Drifts Evidence for Facet-Dependent Adsorption of Gaseous Toluene on TiO_2 with Relative Photocatalytic Properties. *Langmuir* **2015**, *31*, 1730–1736.
- (45) Yashima, M.; Lee, Y.; Domen, K. Crystal Structure and Electron Density of Tantalum Oxynitride, a Visible Light Responsive Photocatalyst. *Chem. Mater.* **2007**, *19*, 588–593.
- (46) Huang, M.; Weng, S.; Wang, B.; Hu, J.; Fu, X.; Liu, P. Various Facet Tunable ZnO Crystals by a Scalable Solvothermal Synthesis and Their Facet-Dependent Photocatalytic Activities. *J. Phys. Chem. C* **2014**, *118*, 25434–25440.
- (47) Zhu, J.; Fan, F.; Chen, R.; An, H.; Feng, Z.; Li, C. Direct Imaging of Highly Anisotropic Photogenerated Charge Separations on Different Facets of a Single $BiVO_4$ Photocatalyst. *Angew. Chem., Int. Ed.* **2015**, *54*, 9111–9114.